# In-situ high-energy X-ray diffraction investigation on stress-induced martensitic transformation in Ti-Nb binary alloys

L.L. Chang[1], Y.D. Wang[2], Y. Ren[3]

[1] School of Materials Science and Engineering, Shandong University, Jinan, 250061, China

[2] State Key Laboratory for Advanced Metals and Materials (SKLAMM) and the Collaborative Innovation Center of Steel Technology (CICST), University of Science and Technology Beijing, Beijing 10081, China

[3] X-Ray Science Division, Argonne National Laboratory, Argonne, IL 60439, USA

## Abstract

Ti-based alloys are widely used as biomaterials due to their low modulus, good biocompatibility and high corrosion resistance. Mechanical strength combined with elastic modulus of Ti-Nb alloys is determined by compositions and processing routes. The aim of this study is to investigate microstructure evolution, mechanical behaviors of cold rolled Ti-Nb alloys with different Nb contents subjected to different heat treatments. Optical microstructure and phase compositions of Ti-Nb alloys were characterized using optical microscopy and X-ray diffractometre. Mechanical behaviors of Ti-Nb alloys were examined by using tension tests. Stress-induced martensitic transformation in a Ti-30at.%Nb binary alloy was in-situ explored by synchrotron-based high-energy X-ray diffraction (HE-XRD). The results obtained suggested that mechanical behavior of Ti-Nb alloys, especially Young's modulus was directly dependent on chemical compositions and heat treatment process. According to the results of HE-XRD, α " -V1 martensite generated prior to the formation of α " -V2 during loading and a partial reversible transformation from α " -V1 to β phase was detected while α " -V2 tranformed to β completely during unloading.

**Keywords:** Ti-Nb alloys; Microstructure; Mechanical properties; Martensite transformation

# 1. Introduction

The Ti-based alloys have been widely used as biomaterials due to their high corrosion resistance, good compatibility, high strength and low Young's modulus [1, 2]. The β-type Ti alloys exhibit a martensitic transformation from β (disordered bcc) to hexagonal martensite (α') or orthorhombic martensite (α″ ), which depends mainly on the alloy composition and materials processing [3-5]. The shape memory effect and superelastic behavior was previously reported in the Ti-Nb, Ti-Mo and Ti-V based alloys [6-9]. However, the Ti-Mo based alloys are susceptible to the formation of brittle ω phase, while the Ti-V alloys are not suitable for biomaterial applications due to the toxicity of V element to human body. Therefore, the Ti-Nb alloys have attracted more attention as a promising biomaterial exhibiting the shape memory effect, superelasticity, and low Young's modulus.

The phase transformation in metals and alloys has been investigated extensively in theory and experiment [5-13]. In order to design and modify the mechanical response of Ti-Nb alloys for biomaterial application, the in-depth understanding of the microstructure evolution and phase transformation behavior during deformation is required. The shape memory effect accompanied by the phase transformation from α″ to β in the Ti-35wt.% Nb alloy binary alloys was first revealed by Baker [10, 11]. Recently, the low modulus and superelasticity of metastable β titanium alloys was elucidated by a continuous phase transformation from β to α″ during loading [8]. The previous studies indicated that the deformation mechanisms in the Ti-Nb system alloys were quite complex, which are closely related not only to the stability of the β phase but also to the detailed scenario of deformation process [8]. It was also postulated that some deformation mechanisms different from the classical martensitic transformation existed in the Ti-Nb alloys. However, so far the detailed deformation mechanisms during the elastic/quasi-elastic stage in the Ti-Nb alloys are not well revealed. The aim of this paper is to investigate the relationship between microstructure and mechanical properties of Ti-Nb alloys and the stress-induced α″ martensite was studied by using the in-situ synchrotron

high-energy X-ray diffraction (HE-XRD). The evolution of lattice strain and phase transformation kinetics vs. applied stress in the Ti-30at.%Nb (noted as Ti-30Nb) alloy were in-situ traced during tensile loading and unloading.

## 2. Experiment

The Ti-20at.% Nb(Ti-20Nb) and Ti-30at.% Nb(Ti-30Nb) alloys were fabricated by an arc melting method under Ar atmosphere and button ingots were prepared. All ingots were melted 6 times to ensure complete dissolution of Nb. After casting, those ingots were sealed in a vacuum in a quartz tube and homogenized at 1000℃ for 3.6ks, and then hot-rolled to sheets. The hot-rolled sheets were cold-rolled at room temperature with a reduction of 90% in thickness and the final thickness of the sheets was about 1 mm. Specimens for optical microstructure observation, X-ray diffraction (XRD) and tension were cut using an electro-discharge machine. The specimens were cleaned with ethanol and encapsulated in quartz under a 25 Torr partial pressure of high-purity Ar to avoid oxidation during solution treatment. Solution heat treatments of Ti-Nb alloys were conducted at 750℃, 850℃ and 950℃ for 3.6 ks, respectively. Optical microstructure of Ti-Nb alloys was revealed by using an etchant of HF(5vol.%) +$HNO_3$(5vol.) + water(bal.). XRD measurements were conducted at room temperature using a Rigaku D/MAX diffractor with Cu-Kα radiation ( $\lambda$ =1.5406 Å) operating at 40 kV and 30 mA. Tensile tests were carried out at a strain rate of $1.0\times10^{-3}$ $s^{-1}$ at room temperature. The gauge length of specimens was 20 mm, and triplicate tests along rolling direction (RD) were conducted. The fracture morphology was observed using scanning electron microscopy (SEM) Quanta FEG 250 operated at 15 kV.

In-situ synchrotron-based HEXRD experiments were performed for studying the mechanical behavior of the Ti-Nb alloy, using the beam-line 11-ID-C at the Advanced Photon Source (APS) at Argonne National Laboratory. An intense monochromatic X-ray beam with the energy of 115 keV (wavelength of 0.10801 Å) and a beam size of 400×400 $\mu m^2$ was used to map the lattice strain distributions of the specimens under the

tensile loading mode. The dog-bone-shaped specimen was first mechanically ground, then mounted on a stress rig implemented at the sample holder with X-Y-Z transmission for in-situ experiments. At different loading levels, the diffraction patterns were recorded on a two-dimensional (2D) detector, which was placed at about 2.1 m behind the sample. The $CeO_2$ powders were attached to the surface of the measured specimen for calibrating the accurate distance between the specimen and the geometry position of 2D detector during deformation. During the in-situ experiments, the $CeO_2$ powders were removed from the sample for obtaining clear diffraction patterns. The lattice strain evolution of Ti-Nb alloy was investigated by tracing the change in lattice spacing with increasing applied load, i.e., $\varepsilon_{hkl} = \frac{d_{hkl} - d_0}{d_0}$, where $\varepsilon_{hkl}$ is the lattice strain of the *hkl* plane and $d_0$ is the interplanar spacing of the specified lattice reflection in a stress-free material. In the current work, the measurement prior to loading was taken as the stress-free state of the specimen. The interplanar spacing of the *hkl* plane, $d_{hkl}$, is obtained in terms of Bragg's law, i.e., $d_{hkl} = \frac{\lambda}{2\sin\theta_{hkl}}$ where $2\theta_{hkl}$ is the diffraction angle of a Debye cone. The Bragg angle $\theta_{hkl}$ of the *hkl* plane was determined by fitting the individual single peak or overlapped peaks in the diffraction spectra with General Structure Analysis System (GSAS) software.

## 3. Results and discussion

### 3.1 Microstructure evolution

Optical microstructures of Ti-Nb binary alloys obtained by quenching into water from different solution treatment temperatures were shown in Fig. 1. As seen in Fig. 1(a-c), α″ martensite plates nucleated and distributed homogeneously inside β grains.The average β grain size of Ti-20Nb alloys solution treated at 750℃, 850℃ and 950℃ was determined to be about 55 μm, 114 μm and 162 μm, respectively. Unlike (β+α″) microstructure of Ti-20Nb, the microstructure of solution treated Ti-30Nb alloys showed single β

phase grain structure and the average β grain size of Ti-30Nb after solution treatment at 750℃, 850℃ and 950℃ was ~51 μm, ~60 μm and ~65 μm, respectively. Those results indicated that for both Ti-20Nb and Ti-30Nb specimens, the grain growth of β occured during solution treatment at high temperature and the grain size increased with the increasing solution treatment temperature. The stability of bcc β phase in Ti-M alloys (M=trainstition element) can be understood from two aspects [12]: (1) the formation energies of compositions, i.e. decrease in formation energy indicates increase in stability of the phase; (2) the ratio of valence electrons and number of atoms (e/a), β phase in Ti-M alloys is stablized at the e/a ratio is 4.2 or more. Karre et al. calculated the binary Ti-Nb systms using first-principles calculations with density-functional framework, the theoretical results suggest that the Ti-Nb alloy system have stable bcc (β) phase for Nb content 22 at.% and higher [12]. However, according to Bönisch et al., β phase was detected in Ti-29wt.%Nb (Ti-18at.%Nb) alloys solution treated at 670 K+WQ (water quenched), 818 K+WQ, 1420 K+WQ [13], which indicated the stability of β phase was significantly influenced by heat treatment process. For our case, α″ and β phases were both observed in the optical microstructure of cold and solution treated Ti-20Nb alloys, the existence of β was also confirmed by the XRD results, as seen in Fig.2 (a). Further investigation of optical microstrucutre indicated that the average β grain size of Ti-30Nb was not sensitive to solution treatment temperature as Ti-20Nb samples do. Previous experimental work suggests that solutes have great influence on grain boundary mobility and hence on the growth rate of recrystallizing grains [13]. Usually, the solute is attracted to the grain boundary and solute segregation occurs, the solute atoms can induce a “solute drag” force on the moving boundary. Therefore, the usual effect of solutes is to hinder recrystallization. For our case of Ti-Nb alloys, the solute Nb atom influences the mobility of grain boundaries by solute drag. When the Nb content was increased, the resistance for the grain growth was increased, which resulted in the insensitivity of grain size to solution temperature, as shown in Fig. 1.

XRD patterns of Ti-Nb alloys in cold rolled and solution treated states were shown in Fig. 2 and lattice

parameters calculated from XRD results were summarized in Table 1. XRD diffraction peaks of cold rolled and solution treated Ti-20Nb alloys were indexed as β and α″ phases, indicating that the martensitic transformation finish temperature ($M_f$) of Ti-20Nb alloys was lower than the room temperature (RT), while the martensitic transformation start temperature ($M_s$) was higher than RT. According to the XRD results, the lattice parameter of β in cold rolled Ti-20Nb alloy was determined to be $a_\beta$=3.27136 Å, while those of the α″ phase were determined to be $a_{\alpha''}$ = 3.08046 Å, $b_{\alpha''}$ = 4.83001 Å and $c_{\alpha''}$ = 4.72561 Å. For cold rolled and solution treated Ti-30Nb alloys, all diffraction peaks were indexed as β phase and its lattice parameter decreased slightly with increasing the solution temperature. Previous studies have revealed that the lattice of constants of phases in Ti-Nb alloys strongly depend on the Nb content of the alloys. The Nb content dependence of the β and α″ orthorhombic martensite in Ti-Nb alloys was reported by Kim et al. [14]. According to their results, the lattice constant of the β phase slightly increases by $0.013\times10^{-3}$ nm/1 at.% Nb in the Ti-(22-35)at.% Nb alloys and the lattice constant of β phase in cold-rolled Ti-22at.%Nb and Ti-30at.% Nb was determined to be 3.2861 Å and 3.2872 Å, respectively. In the present study, the lattice constant of β phase in cold-rolled Ti-20Nb was 3.27136 Å, and it increased to be 3.2901 Å in cold-rolled Ti-30Nb alloys by 0.6% increment, which is close to the results of Kim et al. On the other hand, the lattice constant of β phase in cold rolled and solution treated Ti-Nb alloys was in the range of 3.2901~3.2838 Å , which also agreed well with Kim's results [15]. Besides alloy compositions, the type and lattice constants of phases are also extremely dependent on heat treatment process and the thermal stability. Phase evolution during heat treatment of martensitic Ti-Nb alloys was investigated by a number of authors [7, 13, 16, 17]. Our work indicated that the lattice parameter of β in Ti-30Nb alloys decreased by $2.05\times10^{-6}$ Å/℃ with the increasing solution treatment temperature, as shown in Table 1. For the case of Ti-30Nb alloys, the value was determined to be $1.855\times10^{-5}$ Å/℃, which is almost ten times of the value of Ti-20Nb alloys. Two main factors could have possibly caused the change of lattice constants of phases during heating: (ⅰ) atom

dissolving and (ii) misfit accomodation [18]. As discussed above, conversion of β into α″ martensite happened during quenching of Ti- 20Nb alloys, while the Ti-30Nb alloys kept a single β phase microstructure during quenching and heating. The lattice constant misfit between β and α″ would obviously influence the changing of lattice constant of β phase. The martensite transformation in Ti-20Nb alloys during water quench devided the β grains and induced "refining" of β grains actually. The changing of β lattice parameter was restricted by α″ martensite transformation via misfitting and refining, which resulted in insensitivity of β grain size to the solution temperature.

## 3.2 Mechanical properties

Stress-strain curves for Ti-20Nb and Ti-30Nb alloys in cold rolled state and solution treated states were shown in Fig. 3. The values of Young's modulus (E), yield stress ($\sigma_{0.2}$), ultimate tensile stress ($\sigma_b$) and elongation-to-failure ($\delta$) for samples of Ti-20Nb and Ti-30Nb alloys were determined and listed in Table 2. According to the results, the cold rolled samples showed largest Young's moduli, highest YS and UTS, but lowest elongation, which is the result of the work hardening during cold rolling. After solution treatment at different temperatures, the Young's modulus, YS and UTS of Ti-Nb alloys decreased, while the elongation increased significantly. It should be noted that strengths of Ti-20Nb alloys exhibited abnormal Hall-Petch relationship: the β grain size increased with increasing tempearture of solution treatment, while the YS and UTS increased too. Based on the analysis of optical microstructures of Ti-20Nb samples, the amount of α″ martensite increased significantly with the increasing temeperature, therefore, the spacing of α″ phases decrease largely, which induced hardening of Ti-Nb alloys against the softing of larger β grain size. The combined tensile properties of Ti-20Nb and Ti-30Nb alloys solution treated at 850 ℃ were better among all the corresponding Ti-Nb samples. The Young's modulus of Ti-20Nb alloys solution treated at 850 ℃ was slightly larger than that of Ti-30Nb alloys solution treated at 850 ℃, while the UTS was much larger than those of Ti-30Nb alloys in solution treated conditions. It is also interesting to note that the elongation of

Ti-20Nb alloys after solution treated at 850 ℃ was the largest among all the Ti-Nb samples.

The elastic modulus of materials is one of the intrinsic natures of materials, is determined by the bonding force among atoms. The Young's mudulus of Ti-Nb alloys was reported to be profoundly influenced by the Nb content and the presence of phases. According to previous report from Ozaki et al., a minimum in Young's modulus was observed at the composition of Ti-26at.% Nb (Ti-40%Nb in mass) quenched from the β region [19]. Lee et al. reported a strong dependence of E on the chemical composition and the minimum of E was observed near a compostion of Ti-35wt.%Nb [20]. For various phases of Ti alloys, in general, $E_{\beta} < E_{\alpha''} < E_{\omega}$ [21]. Sun et al. calculated the phase stability, electronic structure and elastic constants of β, α″ and ω metastable phases in Ti-25at.%Nb alloys by first-principles calculations [6]. Their results indicated that in the Ti-25 at.% Nb alloy the $\omega$ phase has the highest Young's modulus among $\beta$, α″ and $\omega$ metastable phases, and the α″ martensite has higher Young's modulus than the $\beta$ phase. In the present study, combing with the XRD results, it can be considered that Ti-30Nb alloys have lower modulus due to their microstructures of a single β phase, and α″ phase contributes to the higher modulus of the Ti–20at.%Nb alloys. Further investigation of strain-stress curves of Ti-Nb alloys indicated that the work hardening in Ti-20Nb alloys was much larger than that in Ti-30Nb alloys. The reason is that α″ phase in Ti-20Nb alloys divided larger β grains and thus reducing the effective slip distance of dislocation and thereby raised the work hardening rate via Hall-Petch equation. It is interested to note that a plateau was observed in tensile curves of both Ti-20Nb and Ti-30Nb samples solution treated at 750 ℃. The plateau due to double yielding was considered to be related to stress-induced α″ martensite transformation [22].

As discussed above, the Ti-Nb alloys with different Nb contents after solution treatment at 850 ℃ showed better combined tensile properties. For further investigation, SEM observation of fracture surfaces of Ti-Nb alloys in solution condition was conducted and tensile fractographic structures of Ti-Nb alloys solution treated at 850 ℃ were shown in Fig. 4. It was seen that the fracture surface of Ti-20Nb solution

treated at 850 ℃ exhibited a dimpled morphology and cleavage fracture surface, while the fractographic structure of Ti-30Nb solution treated at 850 ℃ was shown to be a finely dimpled morphology due to the small average grain size of single β phase microstructure, which is the character of ductile fracture of metals. By way of contrast the fracture surface of Ti-20Nb has a coarse dimpled morphology, which was related to the (β+α″ ) duplex phase microstructure with relatively large β grains.

### 3.3 Scenario of β to α " transformation in Ti-30Nb alloys

As the HE-XRD technique has a high resolution, the direct experimental observation of the stress-induced martensite transformation is possible, which will favor for understanding lower Young's modulus in Ti-Nb alloys. Fig. 5 shows the 2D diffraction patterns together with the integrated one-dimensional (1D) patterns of the Ti-30Nb alloy at the stress of 0 MPa (before loading), 498 MPa (at the maximum stress) and 0 MPa (after unloading) along loading direction (LD), respectively. The diffraction patterns at 0 MPa (before loading) were composed of intense rings that can be indexed as the body-centered-cubic (bcc) structure of beta phase (β). No peak belong to any other metastable phases (such as ω，α "，α') was detected, which indicates that after solution treatment at 1123 K for 1 hr, Ti-30Nb alloy was completely composed of a single β phase. When the applied stress was increased to 498 MPa (ε=8.7%), $\{020\}_{\alpha''}$ and $\{021\}_{\alpha''}$ diffraction peaks of martensite α " were detected, as seen in Fig. 5(b) which indicated that stress-induced α " martensitic transformation occurred during the tensile loading. Fig. 5(c) showed peaks of α " remained in the diffraction patterns after the applied stress was removed. However, comparing to the intensities of peaks at 498MPa, the intensities of $\{020\}_{\alpha''}$ and $\{021\}_{\alpha''}$ diffraction peaks decreased slightly indicating that a partial reverse martensitic transformation from β to α " indeed took place during unloading.

Besides the diffraction peaks belong to the deformation-induced α " phase, it is interesting to note that a diffraction peak near $\{110\}_{\beta}$ peak was also detected during the in-situ loading and unloading, as shown in Fig. 6(a). For clarity, diffraction profiles near $\{110\}_{\beta}$ peak at 0 MPa (before loading), 498 MPa (at the

maximum stress) and (d) 0 MPa (after unloading) are highlighted in Fig. 6(b-d), and the peak near $\{110\}_{\beta}$ peak was indexed as $\{002\}_{\alpha''}$, belong to a variant of α " martensite. It was further found that $\{002\}_{\alpha''}$ diffraction peak completely disappeared after the applied stress was removed (Fig. 6d), which suggests that a completely reversible transformation was detected. As discussed above, two variants of α " martensite was detected during in-situ HE-XRD investigation. For easy discussion, the α " martensite variant with the normal direction of $\{020\}_{\alpha''}$ along the loading direction was noted as α " -V1, while those α " martensite variants with orientation of $[002]_{\alpha''}$ parallel to the loading direction were maked as α " -V2.

Our in-situ HE-XRD experiments show the response of lattice strain vs. applied stress for α " variants, as shown in Fig. 7(a). As seen in Fig. 7(a), in the beginning of loading (50-350 MPa), the lattice strain of $\{020\}_{\alpha''}$ did not change obviously. The applied stress was accommodated mostly by the nucleation and activation of α " phase. When the applied stress was increased from 350 to 460 MPa, the lattice strain of $\{020\}_{\alpha''}$ increased linearly with the applied stress due to the elastic deformation of α " phase. When the applied stress increased continuously, the $\{020\}_{\alpha''}$ lattice strain increased abruptly from 2970 με to be 11570 με. The abrupt increment in the lattice strain was considered as the result of phase transformation from β phase to α " -V2 variant. During unloading process, the evolution of $\{020\}_{\alpha''}$ lattice strain was marked as two stages, the first stage (498-460 MPa) was related to the reversible transformation from the α " -V1 or α " -V2 martensite to β phase, while during the second stage (460-0 MPa) the lattice strain decreased linearly with the applied stress, which was attributed to only elastic deformation of α " martensite.

The phase transformation kinetics vs. applied stress, i.e. the evolution of volume fraction for β, α″ , was shown in Fig.7 (b). The α " -V1 martensite was first detected at the applied stress of ~98 MPa, and then the volume fraction of α " increases with the increasing applied stress during tensile loading. When the applied stress was increased to 498 MPa, the volume fraction of the α " -V1 was determined to be ~20%. However, during unloading the volume fraction of α " -V1 decreased significantly. After the sample was

unloaded completely, ~10% of α " -V1 phase remained. For the case of α " -V2 variant, the volume fraction jumped from 0 to ~10.6 % at the applied stress of 460 MPa. After that the value of the volume fraction of α " -V2 sustained until the applied stress was decreased to be ~262MPa. When the macrostress was decreased further, the volume fraction of α " -V2 was decreased abruptly to be ~0. As discussed, the α″ -V1 martensite transformation developed gradually as the applied stress was increased step by step, while α " -V2 variant seemed to form suddenly. In addition, the volume fraction of α″ -V1 martensite decreased with decreasing the applied stress progressively, while the volume fraction of α " -V2 remained a steady value of ~10% during the beginning of unloading and jumped to 0% at 262 MPa. Therefore, the evolution of the volume fractions for all β, α″ variants at different stress states indicated that behavior of α " variants V1 and V2 was entirely different.

A seqence from β to α " -V1 and from β to α " -V2 martensite transformation in the binary alloy was evidenced during tensile loading and unloading. The different phase transformation kinetics was revealed for both kinds of martensite variant. The α " -V1 martensite is generated prior to the formation of α " -V2 during loading. A partial reversible transformation from α " -V1 to β phase occurred firstly while the completely reversible transformation from α " -V2 to β took place later in abrupt way. Our experiments provide the in-depth understanding of martensitic transformation and its relationship with low Young's modulus of binary Ti-Nb alloys.

## 4. Conclusions

Ti-Nb alloys with different Nb contents were fabricated by argon arc melting followed by cold rolling and solution treatments. Optical microstructure and phase composition of Ti-Nb alloys were characterized by optical microscopy, X-ray analysis and HE-XRD, the effect of microstructure on mechanical properties, especially on Young's modulus was discussed. The main results are concluded as follows:

1. Cold rolled and solution treated Ti-20Nb alloys were composed of β and α″ phases, while cold rolled and solution treated Ti-30Nb alloys were composed of a single β phase. The average grain size of β phase in Ti-20Nb alloys increased significantly with the solution temperature, while the average grain size of Ti-30Nb samples showed little sensitivity to the the solid solution temperature.

2. Young's moduli of Ti-30Nb alloys were in the range of 45~67 GPa, which is much lower than those of Ti-20Nb alloys (49~118 GPa). Plateaus due to martensite transformation were observed in tensile curves of Ti-30Nb samples solution treated at 750 ℃. The Ti-Nb alloys with different Nb contents solution treated at 850 ℃ showed lower modulus combined with higher strength.

3. A seqence from β to α " -V1 and from β to α " -V2 martensite transformation in the binary alloy was evidenced during tensile loading and unloading. α " -V1 martensite generated prior to the formation of α " -V2 during loading. A partial reversible transformation from α " -V1 to β phase was detected while α " -V2 tranformed to β completely during unloading.

## Acknowledgement

The work was supported by the National Basic Research Program of China (973 Program) under Contract No. 2012CB619405, the Promotive Research Fund for Excellent Young and Middle-aged Scientists of Shandong Province (No. BS2013CL034), Independent Innovation Foundation of Shandong University (GN2003001), the National Natural Science Foundation of China (Grant No. 51401115), the Fundamental Research Funds for the Central Universities (Grant No. 06111020), and the fundamental research fund by State Key Laboratory for Advanced Metals and Materials (Grant No. 2014Z-01). Use of the Advanced Photon Source was supported by the U. S. Department of Energy, Office of Science, Office of Basic Energy Sciences, under Contract No. DE-AC02-06CH11357.

## References


[1] I.V. Okulov, U. Kühn, J. Romberg, I.V. Soldatov, J. Freudenberger, L. Schultz, A. Eschke, C.G. Oertel, W. Skrotzki, J. Eckert, Materials & Design, 62 (2014) 14-20.
[2] M. Wen, C. Wen, P. Hodgson, Y. Li, Materials & Design, 56 (2014) 629-634.
[3] E. Sukedai, Y. Kitano, A. Ohnishi, Micron, 28 (1997) 269-277.
[4] Y. Ohmori, T. Ogo, K. Nakai, S. Kobayashi, Mater. Sci. Eng. A, 312 (2001) 182-188.
[5] M. Tahara, T. Kanaya, H.Y. Kim, T. Inamura, H. Hosoda, S. Miyazaki, Acta Mater., 80 (2014) 317-326.
[6] J. Sun, Q. Yao, H. Xing, W.Y. Guo, J. Phys.: Condens. Matter (2007 ).
[7] Y.-L. Zhou, D.-M. Luo, Mater. Charact., 62 (2011) 931-937.
[8] T. Maeshima, S. Ushimaru, K. Yamauchi, M. Nishida, Mater. Sci. Eng. A, 438–440 (2006) 844-847.
[9] A. Devaraj, S. Nag, R. Srinivasan, R.E.A. Williams, S. Banerjee, R. Banerjee, H.L. Fraser, Acta Mater., 60 (2012) 596-609.
[10] B. Wang, Z. Liu, Y. Gao, S. Zhang, X. Wang, Journal of University of Science and Technology Beijing, Mineral, Metallurgy, Material, 14 (2007) 335-340.
[11] C. Baker, Metal Science Journal 5(1971) 92-100.
[12] R. Karre, M.K. Niranjan, S.R. Dey, Materials Science and Engineering: C, 50 (2015) 52-58.
[13] M. Bönisch, M. Calin, T. Waitz, A. Panigrahi, M. Zehetbauer, A. Gebert, W. Skrotzki, J. Eckert, Sci. Technol. Adv. Mater., 14 (2013) 055004.
[14] H.Y. Kim, Y. Ikehara, J.I. Kim, H. Hosoda, S. Miyazaki, Acta Mater., 54 (2006) 2419-2429.
[15] H. Ikehata, N. Nagasako, T. Furuta, A. Fukumoto, K. Miwa, T. Saito, Phys. Rev. B, 70 (2004) 174113.
[16] Z. Zhou, M. Lai, B. Tang, H. Kou, H. Chang, Z. Zhu, J. Li, L. Zhou, Mater. Sci. Eng. A, 527 (2010) 5100-5104.
[17] Z. He, M. Liu, Mater. Sci. Eng. B, 177 (2012) 986-991.
[18] M.J. Starink, V.M.F. Abeels, P. van Mourik, Mater. Sci. Eng. A, 163 (1993) 115-125.
[19] T. Ozaki, H. Matsumoto, S. Watanabe, S. Hanada, Mater. Trans., 45 (2004) 2776-2779.
[20] C.M. Lee, C.P. Ju, C. Lin, Joural of Oral Rehabiliation, 29 (2002) 314-322.
[21] A. Panigrahi, M. Bönisch, T. Waitz, E. Schafler, M. Calin, J. Eckert, W. Skrotzki, M. Zehetbauer, J. Alloy Compd., 628 (2015) 434-441.
[22] M. Tahara, H.Y. Kim, T. Inamura, H. Hosoda, S. Miyazaki, Acta Mater., 59 (2011) 6208-6218.

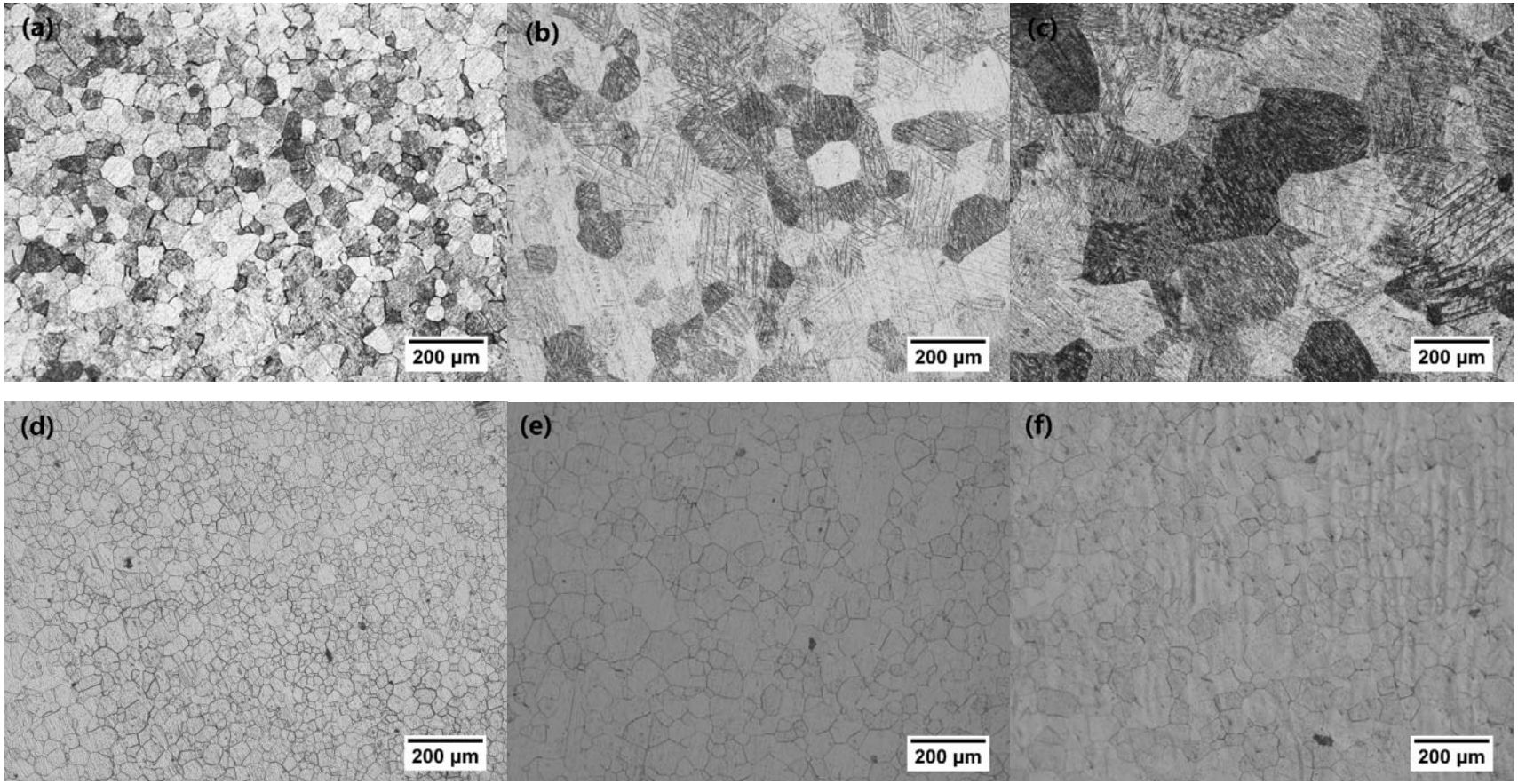


Fig. 1 Optical microstructures of Ti-Nb alloys in solution heat treatment: (a)Ti-20Nb-750℃; (b)Ti-20Nb-850℃; (c)Ti-20Nb-950℃; (d)Ti-30Nb-750℃; (e)Ti-30Nb-850℃; (f)Ti-30Nb-950℃

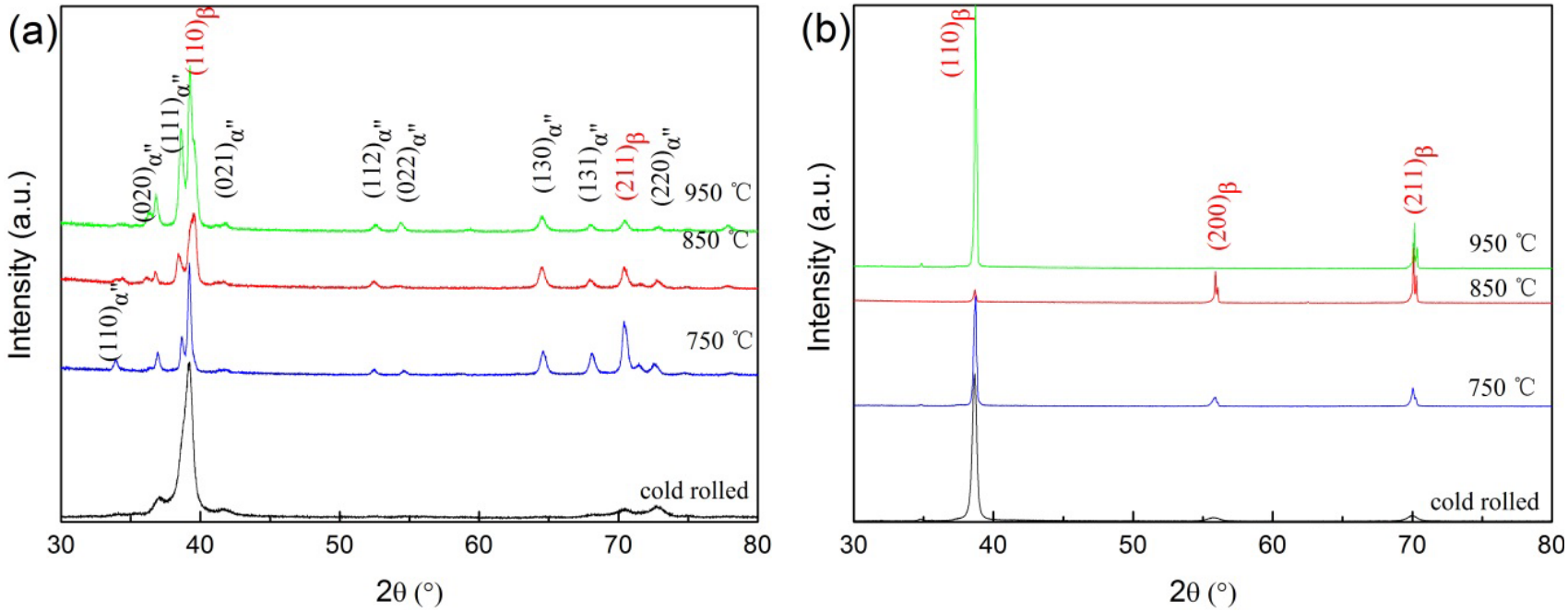


Fig. 2 XRD patterns of Ti-Nb alloys: (a) Ti-20Nb; (b) Ti-30Nb

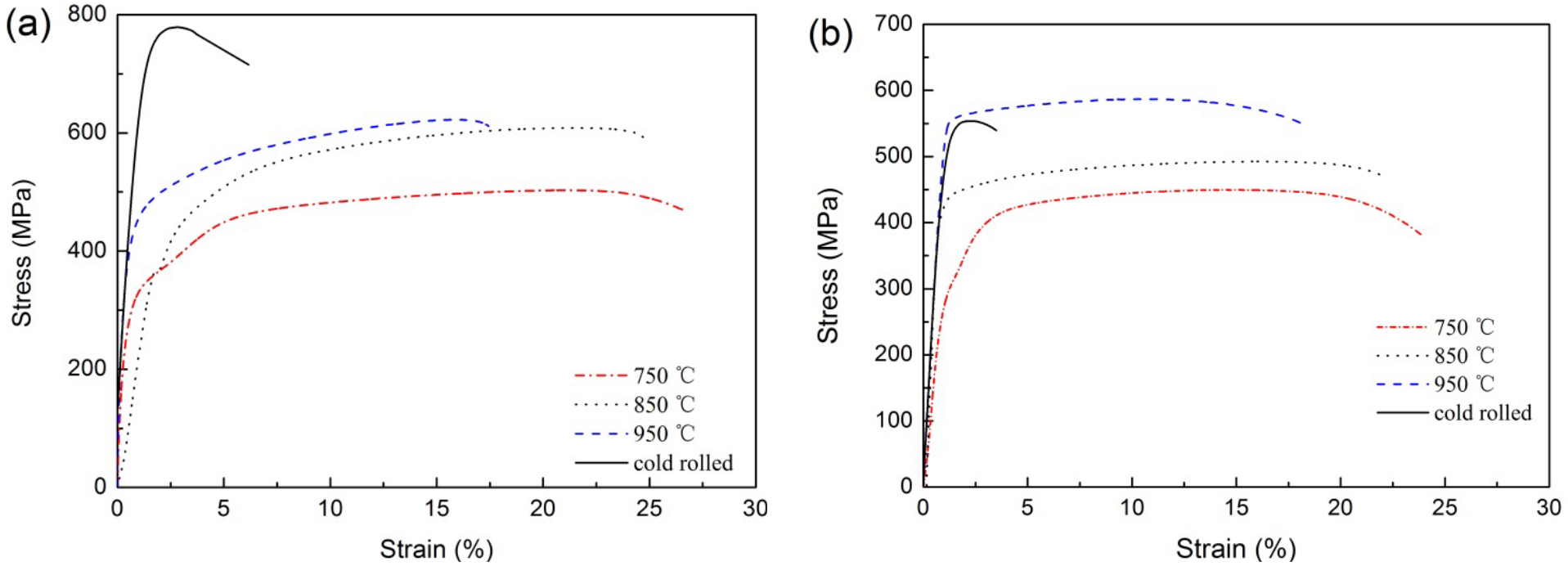


Fig. 3 Tensile strain-stress curves of Ti-Nb alloys: (a) Ti-20Nb; (b) Ti-30Nb

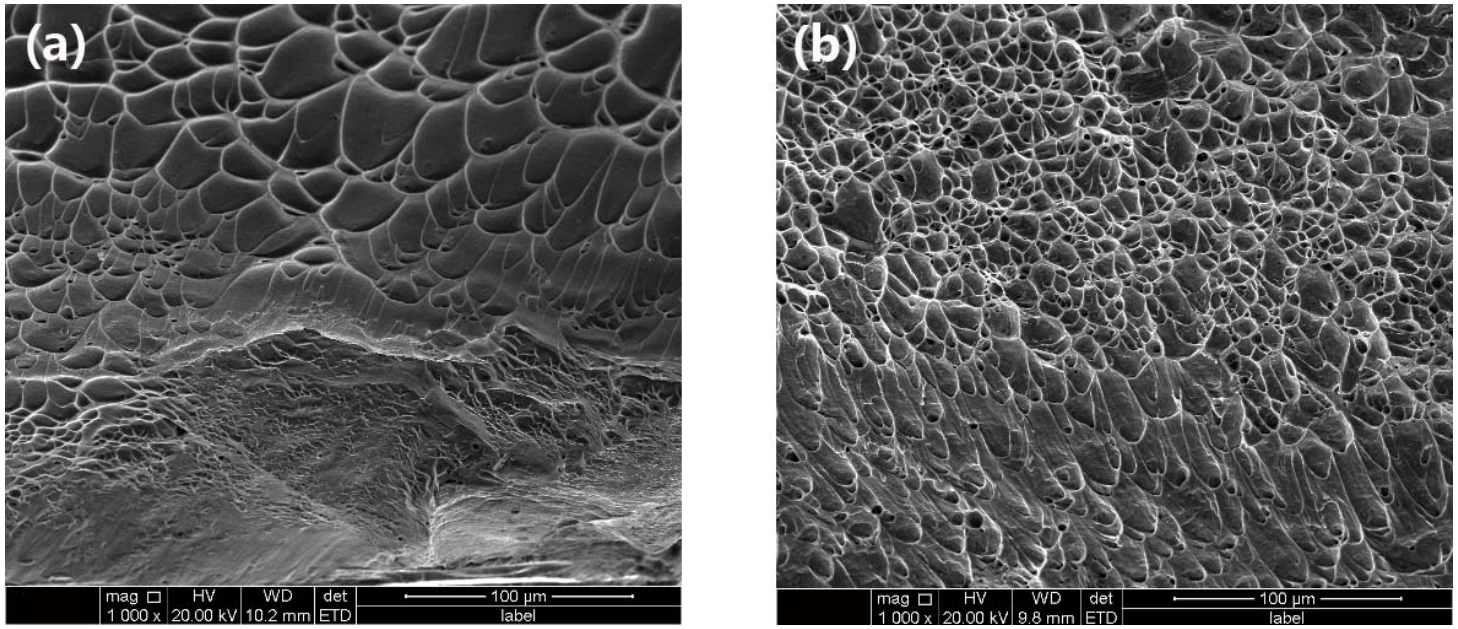


Fig. 4 Fracture surface of Ti-Nb alloys in solution treated conditions: (a)Ti-20Nb-850 ℃; (b)Ti-30Nb-850 ℃

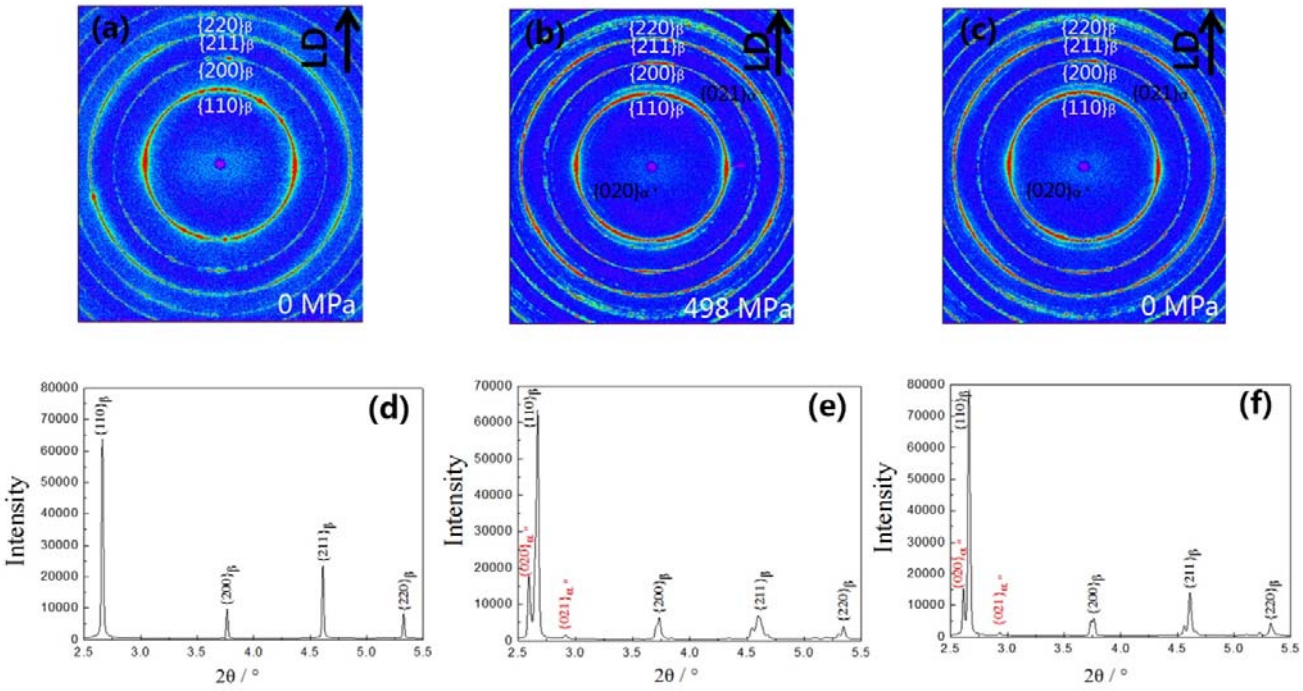


Fig. 5 Two-dimensional X-ray diffraction patterns of Ti-30Nb-850 during in-situ tension: (a) 0 MPa (before loading), (b) 498 MPa (at the maximum stress) and (c) 0 MPa (after unloading) and one-dimensional patterns of the Ti-Nb sample corresponding to different deformation stages along LD: (d) 0 MPa (before loading), (e) 498 MPa (at the maximum stress) and (f) 0 MPa (after unloading).

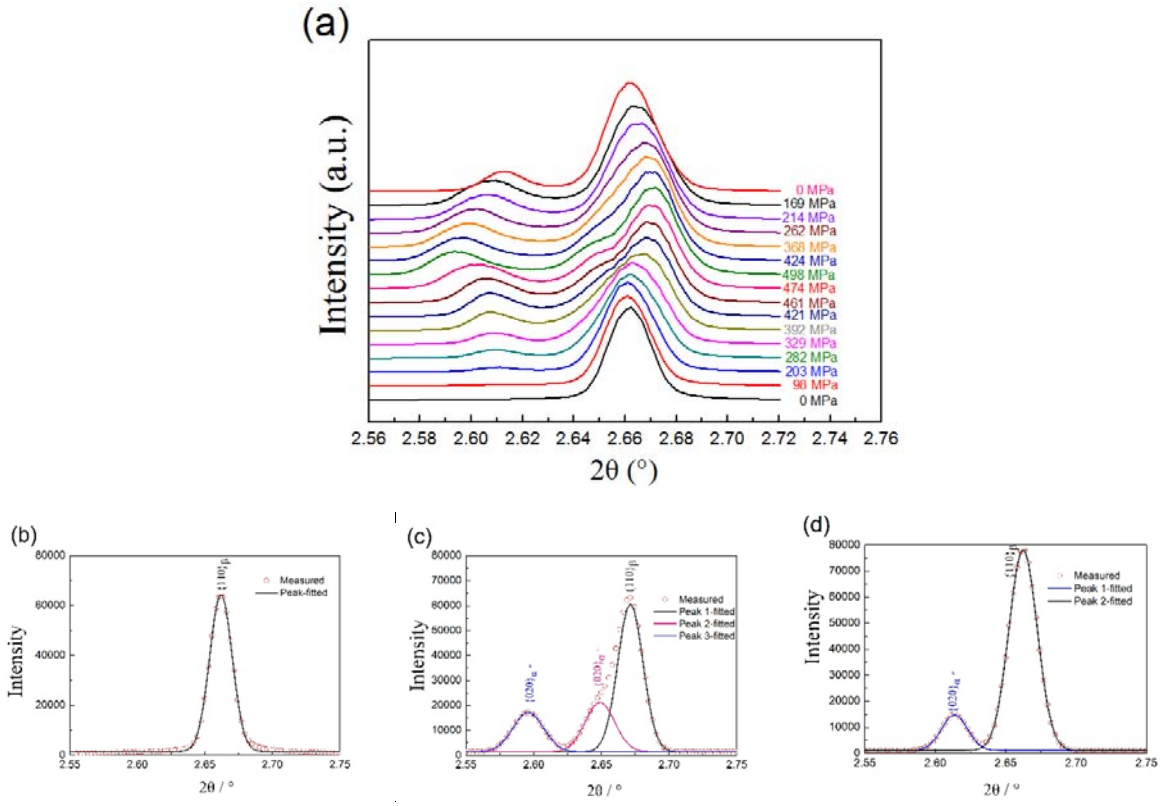


Fig. 6 (a) One-dimensional diffraction patterns of the Ti-Nb sample during in-situ deformation at different applied stressed. The highlighted diffraction profile near $\{110\}_\beta$ peak at (b) 0 MPa (before loading), (c) 498 MPa (at the maximum stress) and (d) 0 MPa (after unloading).

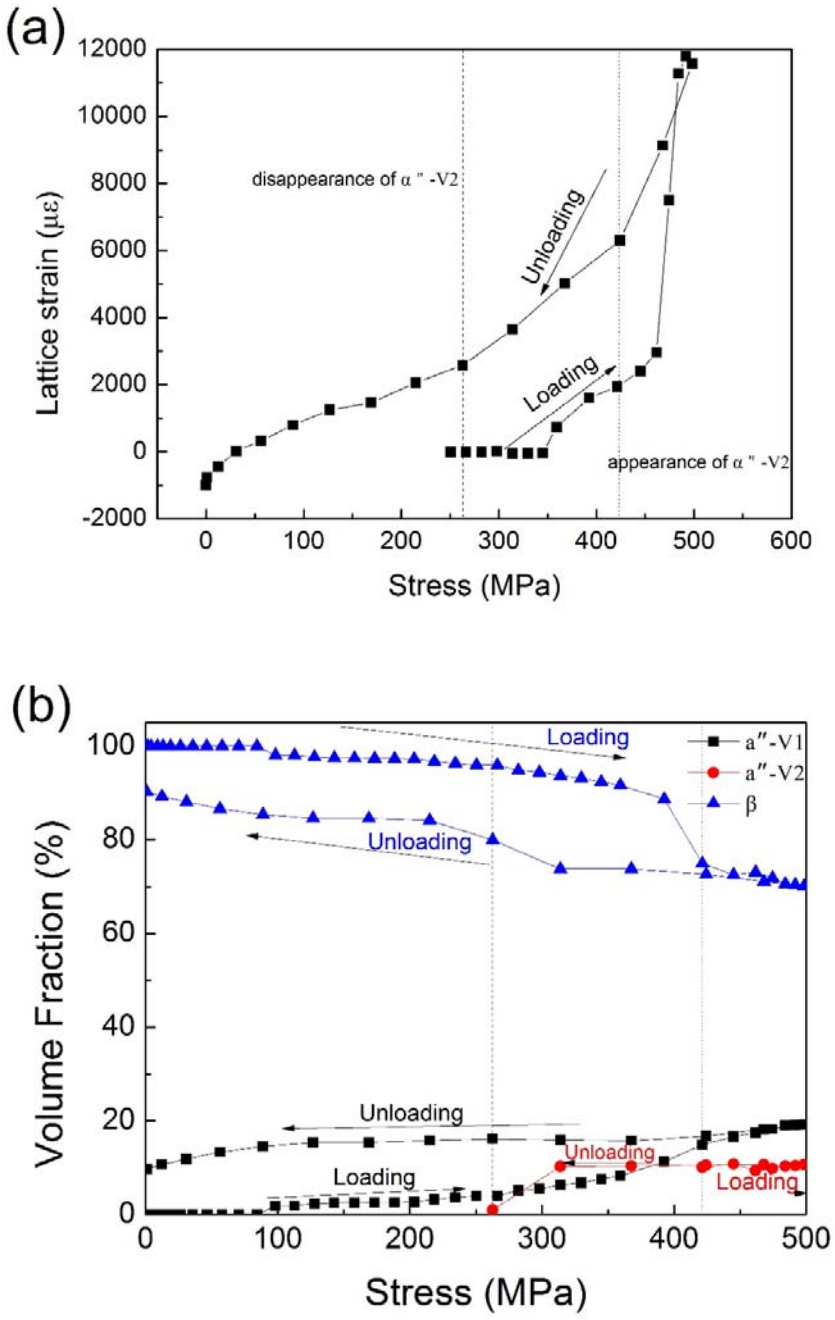


Fig. 7 (a) Lattice strain evolution during in-situ tension for $\{020\}_{\alpha''}$ (LD) and (b) evolution of volume fraction of β, α″ -V1 and α″ -V1 with the macroscopic stress during in-situ deformation